Engineering Fracture Mechanics 319 (2025) 111028

Contents lists available at ScienceDirect

Engineering Fracture Mechanics

journal homepage: www.elsevier.com/locate/engfracmech

Assessing hydrogen embrittlement of alloy 718: Hollow and conventional tensile tests☆

Fabien Ebling [a,b,*], Philipp Bratsch [a], Stefan Wagner [b], Astrid Pundt [b], Johannes Preußner [a], Heiner Oesterlin [a], Ken Wackermann [a], Thorsten Michler [a]

[a] Fraunhofer Institute for Mechanics of Materials IWM, Woehlerstrasse 11, 79108 Freiburg, Germany
[b] Karlsruhe Institute of Technology, Institute for Applied Materials – Materials Science and Engineering (IAM-WK), Engelbert-Arnold-Straße 4, 76131 Karlsruhe, Germany

ARTICLE INFO

Keywords:
Hydrogen embrittlement
Hollow specimen technique
Gaseous hydrogen charging
Alloy 718
Additive manufacturing

ABSTRACT

Testing of metals for hydrogen embrittlement is of great interest for a safe hydrogen infrastructure. However, the costs and efforts involved in in-situ tests in hydrogen pressure autoclaves are high. Simpler alternatives are ex-situ testing with hydrogen pre-charging or in-situ testing with the hollow specimen technique, in which the specimen is pressurized with hydrogen gas from the inside through a longitudinal hole. However, the comparability of the techniques has not been conclusively clarified.

Slow strain rate tensile tests are carried out with the three techniques on the nickel-based alloy 718 in wrought and additive manufactured states. Experiments are performed at hydrogen gas pressures up to 200 bar. Testing in nitrogen gas is used as a reference. Hydrogen pre-charging was conducted at 350 °C and 100 bar pressure. The in-situ techniques show increasing hydrogen embrittlement with increasing hydrogen pressure. The most severe embrittlement could be achieved with hydrogen pre-charging. Conventional and hollow specimens agree on yield strength and tensile strength but differ in elongation to failure and reduction of area. Influencing variables such as surface qualities and multi-axial stresses in hollow specimens resulting from the internal pressure are discussed. The damage mechanisms of all techniques are analyzed by fracture surface examinations using SEM and EBSD.

1. Introduction

Hydrogen embrittlement is of great importance nowadays, as it is crucial to establish a hydrogen infrastructure that is safe and reliable. As early as 1875, W. H. Johnson discovered that hydrogen causes a significant degradation in the structural integrity of steels [1]. Hydrogen diffuses through the metal lattice and interacts with imperfections, such as stacking faults, vacancies, grain boundaries, interphase boundaries, voids and cracks [2–4], resulting in a deterioration of mechanical properties, and often also in a shorter fatigue lifetime of components.

For a safe use of components in hydrogen environments it is essential to determine the relevant mechanical properties under the influence of hydrogen. However, various test methods are used for this, which can lead to differences in the results. Some studies were

☆ This article is part of a special issue entitled: 'Hydrogen Embrittlement' published in Engineering Fracture Mechanics.

* Corresponding author.
E-mail address: fabien.ebling@iwm.fraunhofer.de (F. Ebling).

https://doi.org/10.1016/j.engfracmech.2025.111028
Received 27 August 2024; Received in revised form 20 January 2025; Accepted 7 March 2025
Available online 10 March 2025

Nomenclature

Symbols

ε_f	Elongation to failure
p_i	Inner pressure
p_o	Outer pressure
σ_a	Stress in axial direction
σ_r	Stress in radial direction
σ_t	Stress in tangential direction
σ_v	Equivalent stress
r_i	Inner radius
r_o	Outer radius
r_x	Radius at position x

Abbreviations

AM	Additive manufacturing
BD	Building direction
BMWK	German Federal Ministry for Economic Affairs and Climate Action
BSE	Backscattered electron
CS	Conventional specimen
EBSD	Electron backscatter diffraction
HEE	Hydrogen environment embrittlement
HS	Hollow specimen
IPF	Inverse pole figure
KAM	Kernel average misorientation
LPBF	Laser powder bed fusion
NbC	Niobium carbide
NTS	Notched tensile strength
RA	Reduction of area
SEM	Scanning electron microscope
SLM	Selective laser melting
TiN	Titanium nitride

carried out on hydrogen pre-charged specimens (internal hydrogen) with either gaseous hydrogen pre-charging [5–7] or electrochemical pre-charging [8–12]. The specimens were not always pre-charged to saturation, which leads to an uneven distribution of hydrogen in the specimen [6,9]. Others used in-situ methods (external hydrogen), where hydrogen is provided either gaseous [7,13] or electrochemical [11,14] during the experiment. For applications with gaseous hydrogen, the experiments should also be carried out with gaseous hydrogen to ensure a comparable hydrogen uptake. There are three relevant test techniques for slow strain rate tensile tests with gaseous hydrogen charging:

I. Hydrogen pre-charging: A specimen is first charged with hydrogen in an autoclave and then mechanically tested. As the hydrogen is already in the specimen during experiment, this is also referred to as internal hydrogen.
II. Hydrogen autoclave: These test benches are used to carry out tests on conventional specimen (CS) in a hydrogen atmosphere (external hydrogen) up to high gas pressures. However, this technique is costly, requires high safety precautions and has limitations, such as the applicable temperature and pressure ranges. Another challenge is the load cell, which is located either inside or outside the autoclave. With the first, the difficulty lies in a possible influence of hydrogen on strain gauges [15], and with the second, it lies in subtracting the gas pressure and friction forces from the force signal.
III. Hollow specimen (HS) technique: This technique offers a simple and cost-effective alternative to test under external hydrogen as in autoclaves. It uses specimens with an axial bore hole, which is filled with pressurized hydrogen gas during tensile or fatigue testing. Due to the small volume of hydrogen required for testing with HS, the technique can easily be applied in a laboratory without extensive safety requirements. The technique was already used in 1973 by R.P. Jewet et al. [16] to investigate the compatibility of materials with hydrogen. T. Ogata further developed it and today it is utilized by several institutions [13,17–23]. An advantage of the technology is that the specimen can directly be cooled and heated from the outside during testing [24–26]. However, the technique is not standardized yet and requires further investigation. For instance, tensile tests on various austenitic steels showed a difference between CS and HS in the reduction of area, both for tests in air and in a hydrogen atmosphere, while yield strength and ultimate tensile strength were the same [27]. In addition, various works have been performed to investigate the geometrical influence of the inner bore, of machining procedures and surface qualities [22,27,28].

This work compares tensile properties using CS and HS of nickel-based alloy 718, in both wrought and additive manufactured (AM)

states. The alloy is highly versatile due to its high strength and corrosion resistance, even at high temperatures. Hence, it finds applications in various industries such as aerospace, oil and gas, and chemical processing. In the context of a hydrogen economy, the demand for high-strength materials in hydrogen applications is increasing. However, it is known that high-strength materials are particularly susceptible to hydrogen embrittlement, which leads to a compromise between the properties. The ratio for notched tensile strength (NTS), reduction of area (RA), and elongation to failure (ε_f) tested in hydrogen compared to helium or air is commonly known as the hydrogen environment embrittlement (HEE) index [29]. According to Lee [29], the HEE_{NTS} at 345 bar hydrogen pressure for alloy 718 at various conditions (manufacturing processes, heat treatments and welded metals) is between 0.54 and 0.86 and the alloy 718 can therefore be categorized between "highly" (0.7–0.89) and "severely" (0.5–0.69) embrittled. At 689 bar, it can even be categorized as "extremly" (0–0.49) embrittled with a HEE_{NTS} of 0.46 [30]. For a safe use of components under gaseous hydrogen conditions, it is therefore of particular importance to test the material properties in its specific material condition and under the relevant operating conditions. In addition to the hydrogen pressure, the test temperature should be mentioned here, which also has a strong influence on hydrogen embrittlement and shows a maximum around room temperature for iron and nickel-based superalloys [31].

To gain a deep understanding of the influence of hydrogen pressure on material properties and to make a proper comparison between CS and HS, slow strain rate tensile tests (SSRT) are conducted in air and under hydrogen pressure in a range between 10 bar and 200 bar on alloy 718 in wrought condition. Since additive manufacturing of components is increasingly used due to advantages such as design freedom, material efficiency, and rapid production of small series, specimens are produced additionally using selective laser melting (SLM). These specimens are also tested in SSRT in air, as well as under 10 bar and 100 bar hydrogen gas pressure.

Both, wrought and SLM material are tested in an autoclave and with the hollow specimen technique. In addition, one specimen was pre-charged with hydrogen at 350 °C and 100 bar pressure. In the autoclave, the conventional specimen is tested under hydrostatic pressure, which also causes a hydrostatic stress condition in the specimen. At very high pressures, a hydrostatic pressure of any gas can influence the mechanical properties of a material. However, at the pressures examined here up to 200 bar, these influences are negligibly small [32]. This might be different for the hollow specimen where the cylindrical bore hole is filled with pressurized hydrogen. This causes a multiaxial stress state in the specimen, which might affect the properties determined in the experiment. Hence, possible related effects are investigated in this work as well.

2. Material and methods

2.1. Materials

The investigated materials are nickel based super alloy 718 in wrought condition and additive manufactured by SLM. The powder size of the SLM material was between 10 and 63 μm and the layer thickness in the printing process was 50 μm [26]. Standing blanks were printed with a length of 143 mm in building direction and a diameter of 14 mm. The wrought material was heat-treated according to the standard heat treatment AMS 5663, i.e. solution annealing (941–1010 °C), air cooling and two step precipitation heat treatment (718–760 °C for approx. 8 h and 621–649 °C for approx. 8 h). The exact conditions were not documented. The SLM material was solution annealed at 980 °C for 1 h, air cooling and precipitation heat treated at 720 °C for 8 h and 620 °C for 8 h, also in accordance with AMS 5663.

2.2. Slow strain rate tensile tests

Slow strain rate tensile tests were conducted on conventional specimens in an autoclave system in hydrogen atmosphere, on a hydrogen pre-charged CS and on hollow specimens with inner hydrogen pressure. SSRT were conducted under a constant displacement rate of 0.001 mm/s for HS and 0.0009 mm/s for CS, respectively. Considering the slightly different gauge length, this results in an identical technical strain rate of $3x10^{-5}$ 1/s. The duration of the tests was 1 to 2 h, depending on the elongation to failure. A 1000 bar autoclave test system with a Walter + Bai electromechanical testing machine of type LFMZ and internal load cell was used for the tests on conventional specimens. Experiments with hollow specimens were conducted on a Zwick Roell Kappa DS 150 electromechanical creep testing machine. When tested with hydrogen, the time between the start of the flushing procedure and the start of the mechanical experiment was around 30–60 min. Taking a hydrogen diffusion coefficient of alloy 718 at 20 °C of $D = 8.77x10^{-16}m^2/s$[33] and the penetration depths $x_p = 2\sqrt{Dt}$, the maximum penetration depths prior to testing is 3.55 μm.

Hydrogen pre-charging of the conventional specimen was conducted according to Ebling et al. [34] at 350 °C, a pressure of 100 bar and hydrogen gas of purity 6.0 for 10 days. The charging temperature was chosen so that it is well below the temperature for the formation of γ', γ'' and δ-phase, which starts around 590 °C according to the temperature–time-transformation-diagram of A. Oradei-Basile and J. Radavich [35]. Damage to the material in form of cracks or pore formation caused by pre-charging was also not observed. Before charging was started an alternating pressure flushing between 10 bar and 100 bar with 10 cycles was used to achieve good gas quality. Ebling et al. [34] measured the hydrogen content after 3, 10 and 20 days with a hydrogen analyzer Elementrac OH-p 2 from Eltra. Saturation of the specimens with a diameter of 6.25 mm and a length of 7 mm was reached after 10 days. The measured concentration was 26.9 ± 2 ppm.

The detailed test setup for the hollow specimen technique is shown in Fig. 1. The HS is connected to the specimen fixtures and the assembly consisting of pressure gauge and valves. This setup is filled in a gas station outside the laboratory and is subsequently attached to the testing machine in the laboratory. This means that there is only a small amount of hydrogen in the system and safety

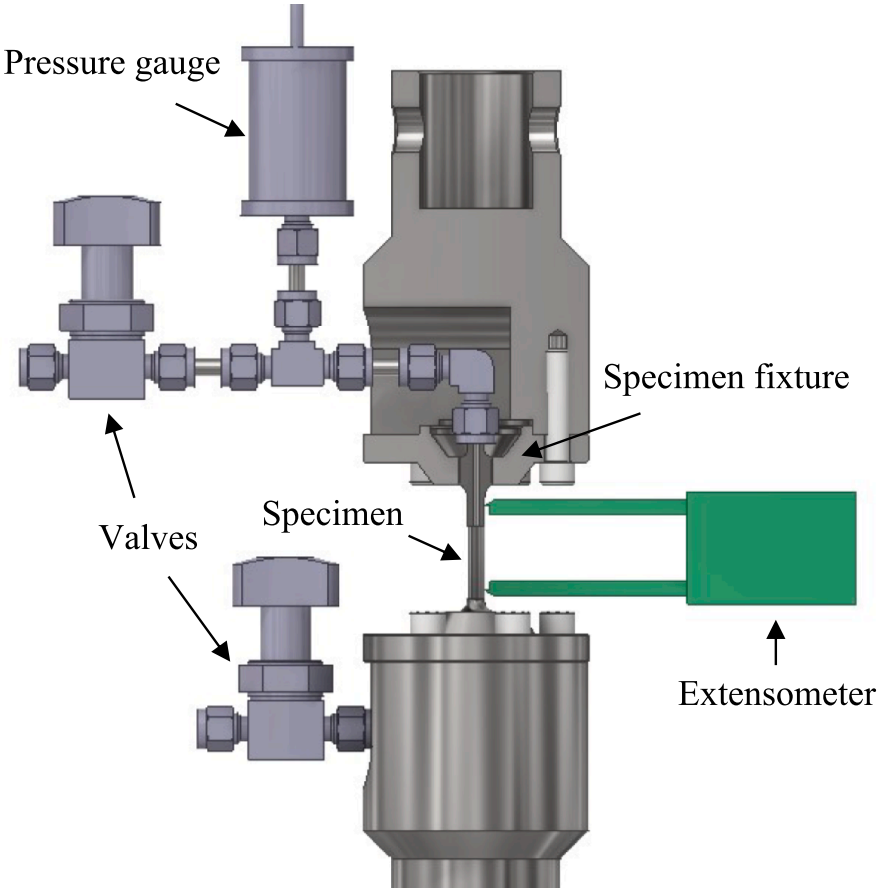

Fig. 1. Test setup for hollow specimens with extensometer, pressure gauge and valves.

precautions in the laboratory can be reduced to a minimum. The flushing procedure used for HS was the same as for pre-charging.

To measure the hydrogen uptake of the material, small changes in the hydrogen pressure were recorded with a Swagelok pressure gauge of type PTI-E-AG160-49AS-D with a pressure range of 0–160 bar and an accuracy $\leq$ 0.5 % of full-scale calibration (0.25 % best fit straight line of the measuring range). To be able to measure potential hydrogen absorption of the specimen more accurately, the gas volume of the system was reduced as much as possible. To achieve this, the pipes were shortened, and additional metal pieces were inserted into the pipes and specimen to reduce the system volume. To measure the volume of the system, it was filled with water and the difference in weight was measured. This procedure and calculation revealed a system volume of 3.6 cm^3. This volume was used for the experiments conducted under 150 bar hydrogen gas pressure. The volume was reduced to 2.8 cm^3 for the experiments conducted under 100 bar hydrogen gas pressure.

Two different specimen geometries (CS and HS) were used for tensile testing, as shown in Fig. 2. For the HS, first a hole was drilled through the blanks of wrought and SLM material by deep hole drilling. To ensure good centering of the hole in the specimen, the drilled blank was clamped on tips and then the final outer contour of the specimen was turned. Finally, the outer surface was polished in the gauge section. The roughness of the outer surface of the hollow specimen and the surface of the inner hole were measured using a Hommel T8000/TKU300 tactile profilometer with traversing length lt = 1.5 mm, cut-off wavelength $\lambda c = 0.25$ mm and measuring speed vt = 0.15 mm/s according to ISO 4287/4288. The roughness of the outer surface was Ra = 0.05 μm and Rz = 0.26 μm. The surface roughness of the drilled hole was Ra = 0.23 μm and Rz = 1.32 μm. Attempts were made to improve the surface quality by honing. Since the roughness could not be improved by honing (Ra = 0.49 μm and Rz = 3.21) μm, all experiments were conducted in as-drilled condition.

2.3. Microscopy

Micrographs were taken with a Nikon Eclipse ME optical microscope. Fracture surfaces were examined with a Hitachi S-3400 scanning electron microscope (SEM) equipped with a tungsten cathode using an accelerating voltage of 20 kV and a secondary electron detector. A Zeiss SEM, model Sigma 300, with an accelerating voltage of 20 kV and an electron backscatter diffraction (EBSD) system from EDAX was used for the analysis of cross sections in the regions of cracks, applying a scan step size of 0.5 μm. The software OIM Analysis™ version 8.6 was used for data evaluation.

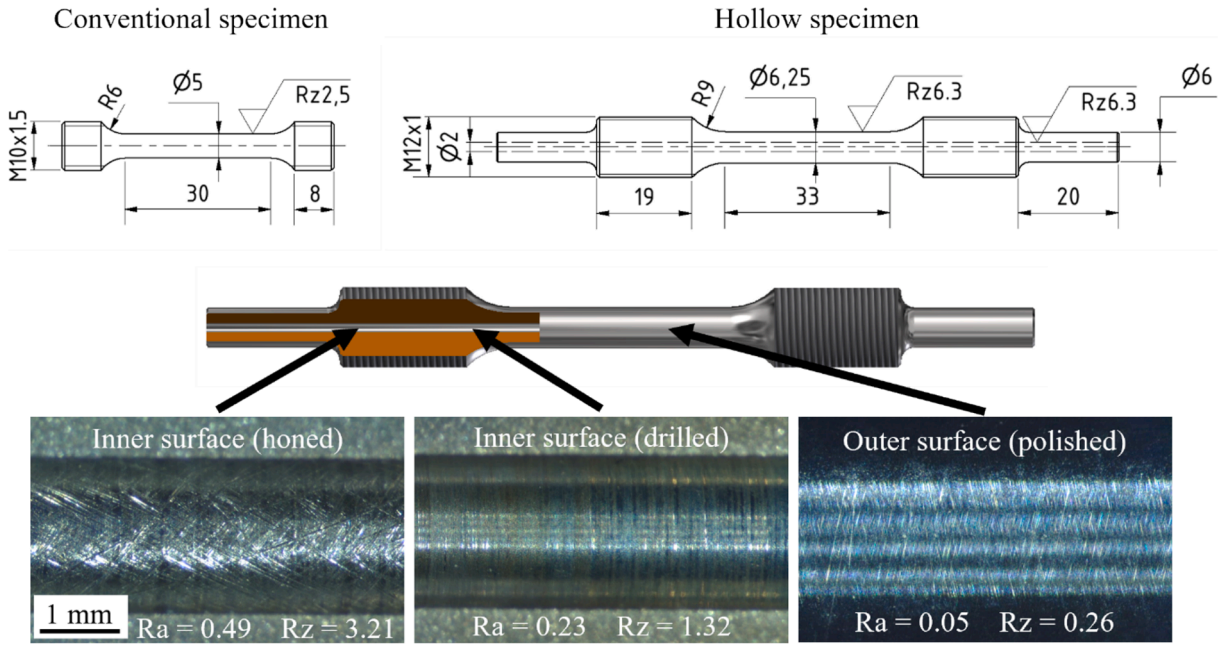

Fig. 2. Geometries of conventional and hollow specimens (top), CAD representation of the hollow specimen (middle) and micrographs of the inner and outer surface of the hollow specimens (bottom). The outer surface of the conventional specimens was processed in the same way as the outer surface of the hollow specimens.

3. Results

3.1. Microstructure

The micrographs in Fig. 3 show the longitudinal and transversal cross sections with respect to the building direction (BD). The longitudinal direction is along the BD for SLM material and along the rod for wrought material. The grains of the SLM material are elongated in the BD (Fig. 3a), while a slight checkered pattern is visible in the transversal section (Fig. 3c). This checkered pattern is

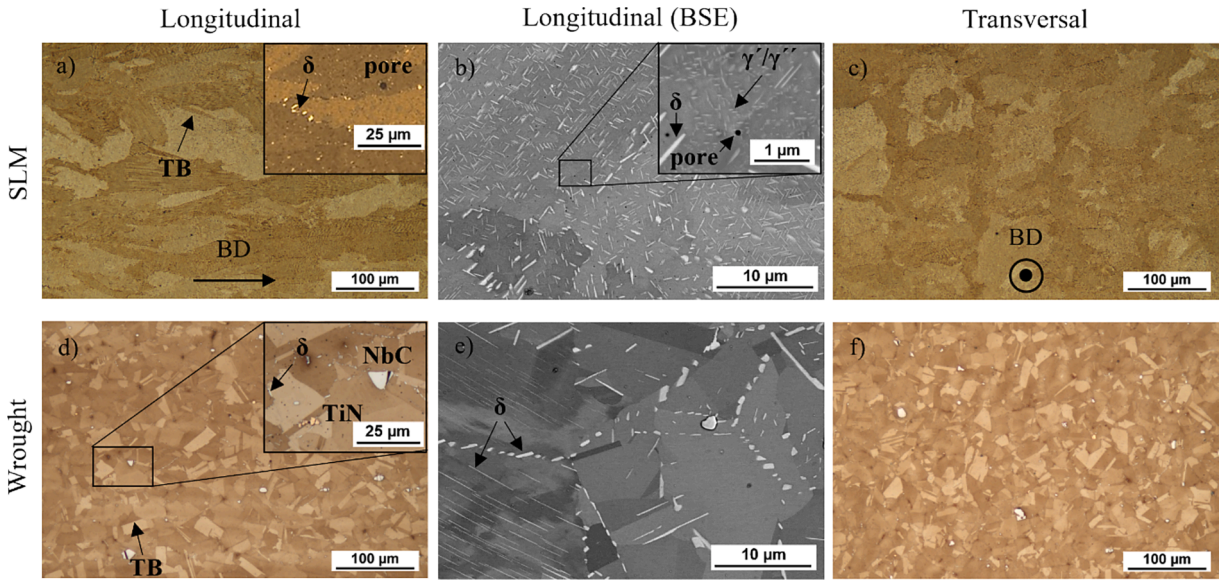

Fig. 3. Micrographs of alloy 718 in both wrought and selective laser melted (SLM) state. For the SLM material, images were taken using a light microscope in both longitudinal (a) and transversal (c) directions relative to the building direction (BD). For the wrought material, images were taken in longitudinal (d) and transversal (f) directions relative to the bar direction. Backscattered electron (BSE) images (b) and (e) were taken using a scanning electron microscope (SEM). Twin boundaries exemplary marked as TB.

created by the laser tracks in the printing process. Additionally, small pores and some delta phase precipitation at the grain boundaries can be observed. The backscattered electron (BSE) image (Fig. 3b) shows that the delta phase has been precipitated both at the grain boundaries and within the grains. At higher magnification, smaller precipitates (approx. 0.03–0.2 μm) can be seen between the larger needle-shaped delta precipitates (approx. 0.4–1.2 μm). Based on the study conducted by Li et al. [36], it can be assumed that these smaller precipitates are γ'' precipitates.

In the case of the wrought material, the grain structure does not exhibit a clear orientation due to the manufacturing process. The grains in the wrought material are slightly smaller compared to the SLM material and have sharper edges, making them more distinct. Twin boundaries, although present in both materials, are more prominently visible in the wrought material. Titanium nitrides (TiN) and niobium carbide (NbC) precipitates were found in the wrought material, but not in the SLM material. The delta phase is primarily observed at the grain boundaries in the wrought material. However, thin, needle-shaped precipitates of the delta phase can also be seen along slip planes in deformed grains (Fig. 3c). γ' and γ'' precipitates were not found for the wrought material, even at higher magnification.

3.2. SSRT on alloy 718 wrought condition

Fig. 4 shows the stress–strain curves of SSRT on CS and HS. For the experiments conducted in ambient air, the strength values $R_{p0.2}$ and R_m match well for HS and the average of CS, with $R_{p0.2,\ HS,air} = 1173$ MPa and $R_{m,\ HS,air} = 1403$ MPa for the HS and $R_{p0.2,CS,air} = 1166 \pm 18.2$ MPa and $R_{m,CS,air} = 1417 \pm 4.8$ MPa for the CS, respectively. The situation is different when the elongation to failure ε_f is considered, which is lower for the HS than for the CS with $\varepsilon_{f,HS,air} = 18.1\,\%$ and $\varepsilon_{f,CS,air} = 22.8 \pm 0.5\,\%$, respectively. The evaluated mechanical parameters of all tests are listed in Table 1.

The experiments on hollow specimens with 100 bar and 150 bar inner pressure of nitrogen gas (grey curve) show values of $R_{m,\ HS,100N_2} = 1406$ MPa, $R_{m,\ HS,150N_2} = 1396$ MPa, $\varepsilon_{f,HS,100N_2} = 19.2\,\%$ and $\varepsilon_{f,HS,150N_2} = 18.4\,\%$. The deviation from the experiment in ambient air (black curve) is small. Therefore, it can be concluded that the influence of an internal pressure on the results is negligible up to a pressure of 150 bar. In contrast, hydrogen has a significant influence on the experiment with increasing pressure. While 10 bar hydrogen pressure (dark blue curves) are negliable, a strong decrease in elongation to failure is observed with increasing hydrogen pressure for both, the HS and the CS. At 200 bar (red curve) the elongation to failure was reduced to $\varepsilon_{f,HS,200H_2} = 7.8\,\%$ and $\varepsilon_{f,CS,200H_2} = 12\,\%$. The hydrogen pre-charged CS (purple curve) elongation to failure was $\varepsilon_{f,CS,charged} = 8.5\,\%$.

The fracture surfaces of the specimens were examined to determine differences in the damage behavior of HS and CS. Fig. 5 presents the fracture surfaces of the CS tested in air, in the pre-charged state and in 200 bar hydrogen atmosphere. The specimen tested in air shows a typical cup and cone fracture (Fig. 5a). In this case, the damage starts in the center of the specimen, characterized by void nucleation, void growth and void coalescence. This area of the fracture surface shows ductile dimples (Fig. 5b). The sheared residual fracture can be seen around this area in the form of typical shear dimples.

For the specimen pre-charged with hydrogen (Fig. 5c, d), it is likely that voids will also initially form in the center. But in contrast to experiments in hydrogen atmosphere, hydrogen is already present in the material and does not have to be absorbed via the surface and diffuse into the volume. Consequently, hydrogen can rapidly diffuse and accumulate at voids, leading to increased damage and crack growth from within the specimen. The fracture surface in this internal region displays both ductile dimples and weakened twin or grain boundaries in the form of flat surfaces. This region is surrounded by a small shear zone. This shear frature occurs during the final break, which takes place very quickly and no hydrogen damage occurs. The crack growth promoted by hydrogen from within also means that necking hardly occurs. For this reason, the $\varepsilon_{f,CS,charged} = 8.5\,\%$ and $RA_{CS,charged} = 12.6\,\%$ are comparatively low.

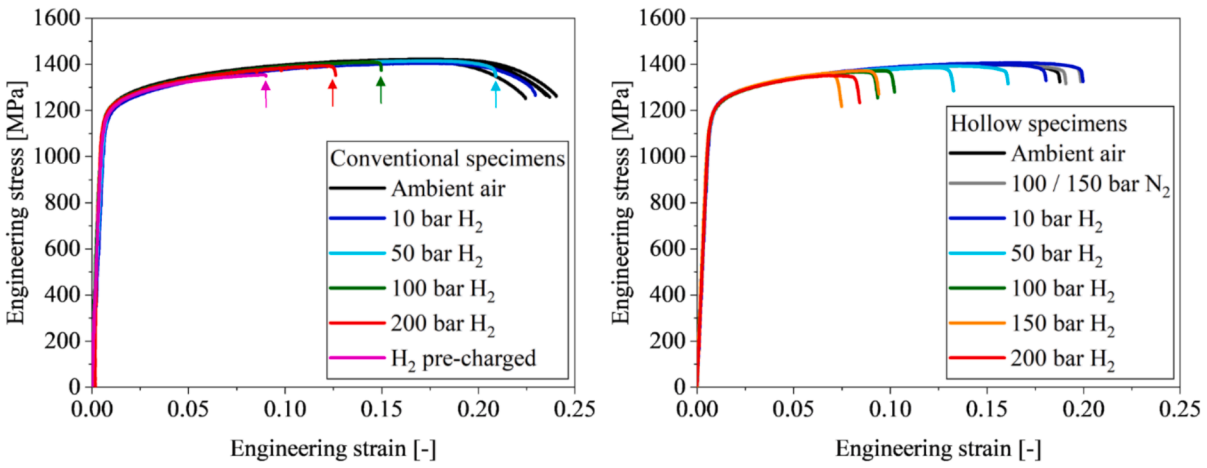

Fig. 4. Tensile tests at different hydrogen gas pressures in autoclave system on conventional specimens (left), pre-charged conventional specimen (left) and on hollow specimens with inner hydrogen gas pressure (right) of wrought alloy 718. Arrows mark the point of failure.

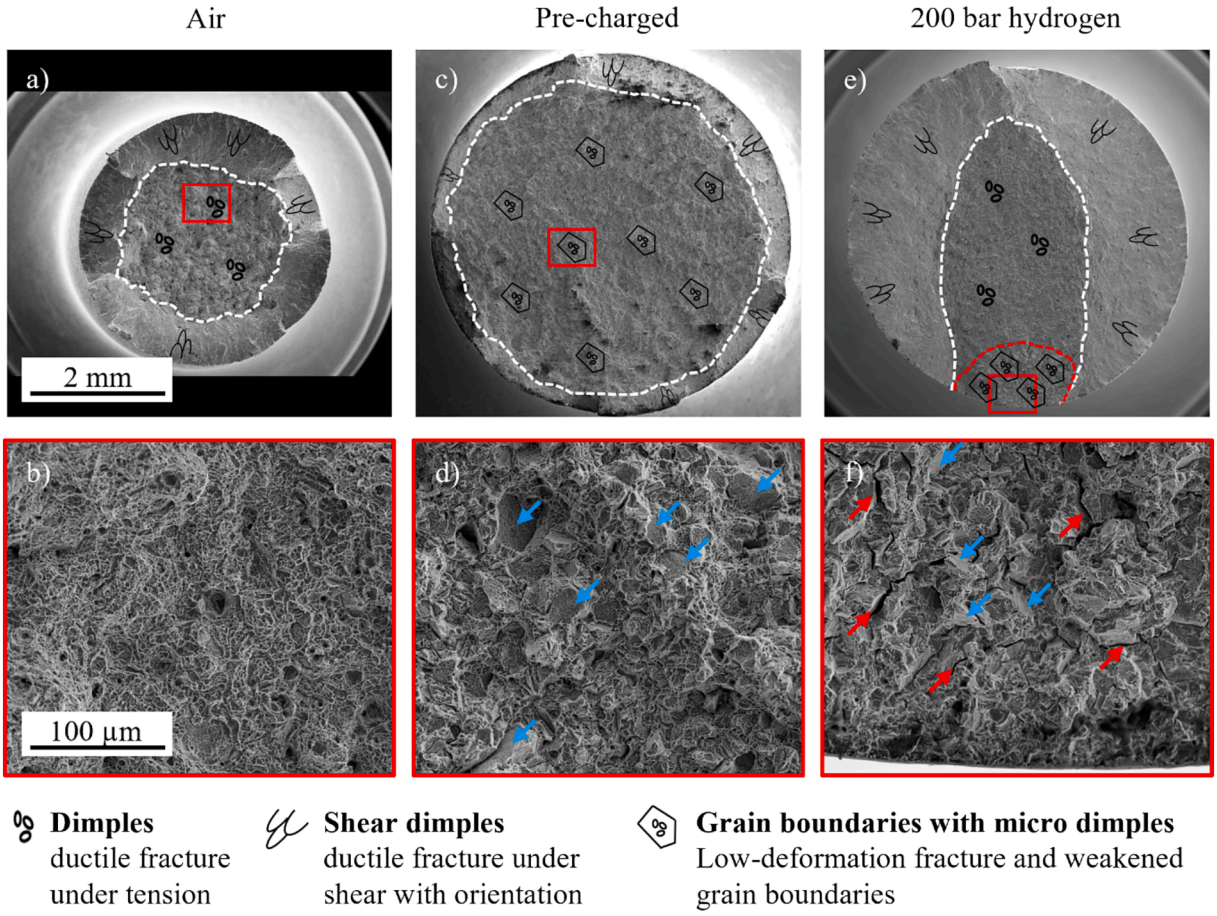

Fig. 5. Fracture surfaces of conventional tensile test specimens in wrought condition tested in air (a, b), hydrogen pre-charged (c, d) and in 200 bar hydrogen gas atmosphere (e, f). (Fractographic symbols based on [37]). Red arrows mark secondary cracks and blue arrows flat surfaces.

In the specimen tested under hydrogen atmosphere (Fig. 5e), void nucleation present in the interior of the specimen without hydrogen competes with hydrogen-favored cracks from the surface. This can be seen by the dimpled ductile area (white line) and the hydrogen-influenced crack starting from the outside (red). This crack shows very low ductility, ruptured grain surfaces and side cracks (Fig. 5f). If a hydrogen-favored crack from the outside reaches a critical length, it grows into the area already damaged by voids. Therefore, the area in the center of the specimen shows a predominantly ductile fracture without hydrogen damage. Finally, the specimen failed by overload as can be seen by the shear fracture. This process is too fast for sufficient hydrogen absorption and to cause an effect of hydrogen on the fracture morphology. Further secondary cracks of brittle nature were observed on the specimen's outer gauge surface.

In principle, the HS (Fig. 6) show a similar damage behavior, which, however, looks slightly different due to the borehole. The fracture surface of the specimen tested in air (Fig. 6 a, b) also shows an area perpendicular to the tensile direction characterized by void nucleation and coalescence. However, this was only on one side and the area was much smaller compared to the solid specimen. The area of residual shear fracture is thus larger. This large area of residual fracture could be an indicator why there is significantly less necking for the HS. This also means that most of the reduction of area is caused by elongation and transverse contraction of the parallel section and not by local necking. The same damage behavior can be seen in the specimen that was tested with 150 bar internal nitrogen pressure (Fig. 6 c, d).

The damage behavior of the HS tested under hydrogen (Fig. 6e, f) appears similar to the CS tested in hydrogen. The hydrogen-induced damage affects the entire circumference of the inner surface of the bore hole exposed to hydrogen, see area marked with a red dashed line in Fig. 6e. This crack then grows into an area damaged by void nucleation and eventually leads to failure again due to shear fracture at the outer circumference. Further secondary cracks can be seen along the gauge surface of the borehole (Fig. 7).

Fig. 7 presents EBSD results on a cross section in the region of a crack on the HS of the wrought material tested in ambient air and with 200 bar inner hydrogen gas pressure. Fig. 7a shows the inverse pole figure (IPF) map of the area around a crack in the specimen tested in air. It exhibits transgranular crack growth at about 45° orientation to the surface. In contrast, the specimen tested in hydrogen, Fig. 7e, predominantly shows transgranular crack growth at about 90° orientation to the surface, with some intergranular crack growth, probably along annealing twin boundaries [38]. It is likely that such intergranular fracture is represented by the flat

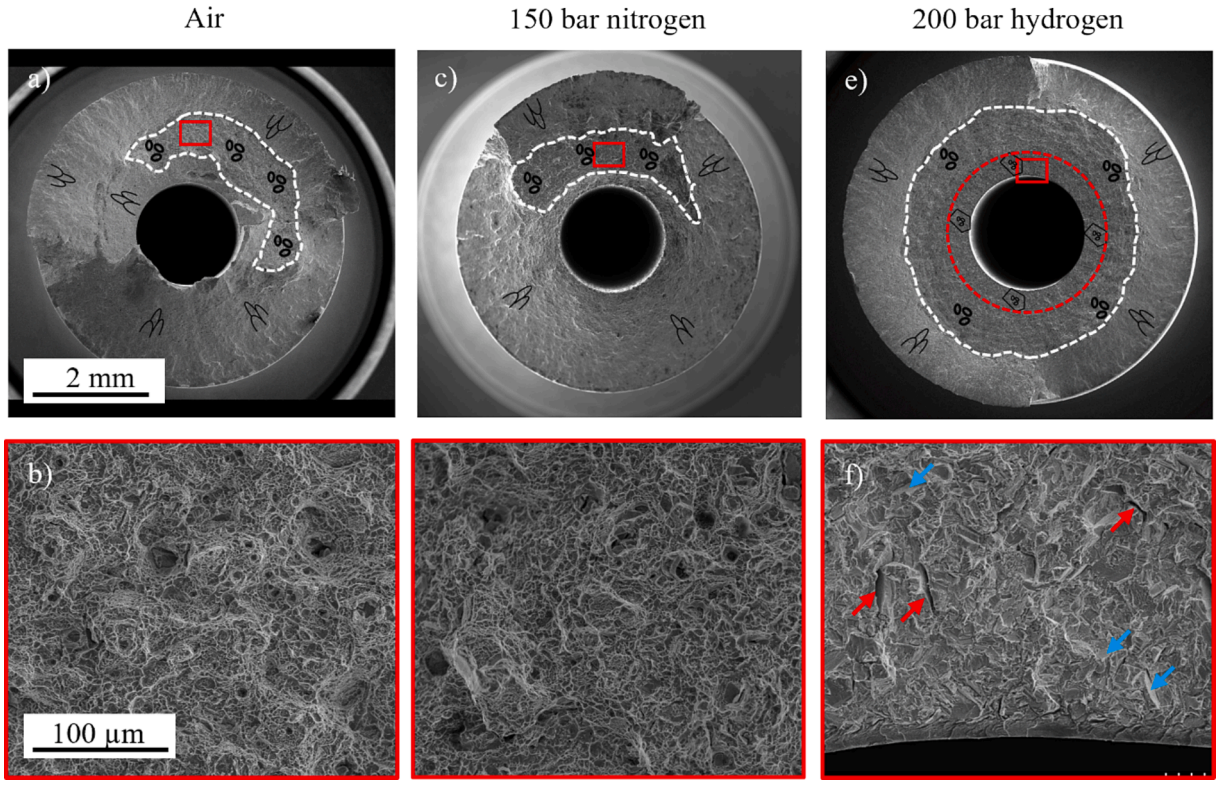

Fig. 6. Fracture surfaces of hollow tensile test specimens in wrought condition tested in air (a, b), with 150 bar inner nitrogen pressure (c, d) and with 200 bar inner hydrogen pressure (e, f). (Fractographic symbols based on [37]). Red arrows mark secondary cracks and blue arrows flat surfaces.

surfaces seen in Fig. 5d and f and Fig. 6f, which were tested with hydrogen. Fig. 7b and f show the kernel average misorientation (KAM) maps of the two specimens, revealing that the specimen tested in air exhibits significantly greater plastic deformation around the crack tip than the specimen tested in hydrogen. Fig. 7c shows a macro image of the failed specimen tested in air, which demonstrates that not only the secondary cracks predominantly grow at a 45° direction, but also the main crack has mostly resulted in a 45° shear fracture. In contrast, Fig. 7g shows that in the hydrogen tested specimen the main crack initially grows in a 90° direction and then results in a 45° shear fracture. This crack growth is schematically depicted in sketches Fig. 7d and h for the two specimens. Overall, significantly more and longer cracks were found in the specimen tested under hydrogen than in the specimen tested in air.

3.3. SSRT on alloy 718 SLM condition

Fig. 8 shows the results of the experiments on the SLM material. Also in this material, the tensile strength of CS and HS is similar, while the elongation to failure of HS is lower than that of CS with $R_{m,\ HS,air} = 1284$ MPa and $\varepsilon_{f,HS,air} = 17.5$ % compared to the CS with $R_{m,\ CS,air} = 1281$ MPa and $\varepsilon_{f,CS,air} = 21.3$ %. Compared to the wrought material, however, the strength and elongation to failure are slightly lower. The results of the tests with hydrogen gas differ significantly between CS and HS. While hydrogen embrittlement is clearly visible for the HS at 100 bar, this is less pronounced for the CS.

The alloy 718 SLM was examined in comparison to the wrought alloy 718 material. It can be seen at the fracture surfaces shown in Fig. 9a and b that, compared to the wrought material, flat surfaces already occur by testing in air and the ductile dimples are a little smaller. In addition, a pore can be seen at the bottom right of Fig. 9b. This pore was caused by the additive manufacturing process.

The CS tested in 100 bar hydrogen (Fig. 9c) exhibits a fracture behavior similar compared to the wrought material. A hydrogen affected brittle region is visible on the top right corner of Fig. 9c. From there the crack grew into a fairly ductile region, in which void coalescence dominated. However, this changes again to a fracture with low deformation and fracture at grain boundaries (Fig. 9d) before the residual shear fracture occurs on the outer circumference. It is assumed that the deeper flat surfaces were not caused by hydrogen, but that the additive material under air with high stress intensities also leads to the fracture of twin boundaries or slip planes, as can be seen in Fig. 9a and b of the air sample. In the HS tested with 100 bar hydrogen gas pressure (Fig. 9e, f), hydrogen damage was observed around the borehole in the form of flat areas and secondary cracks. Inside the wall thickness of the hollow specimen, increasing ductility is visible again in the form of dimples, and close to the outer circumference, shear fracture is observed. In addition, Fig. 9f shows a fracture morphology in the region up to approximately 30 µm below the borehole surface (green area) that

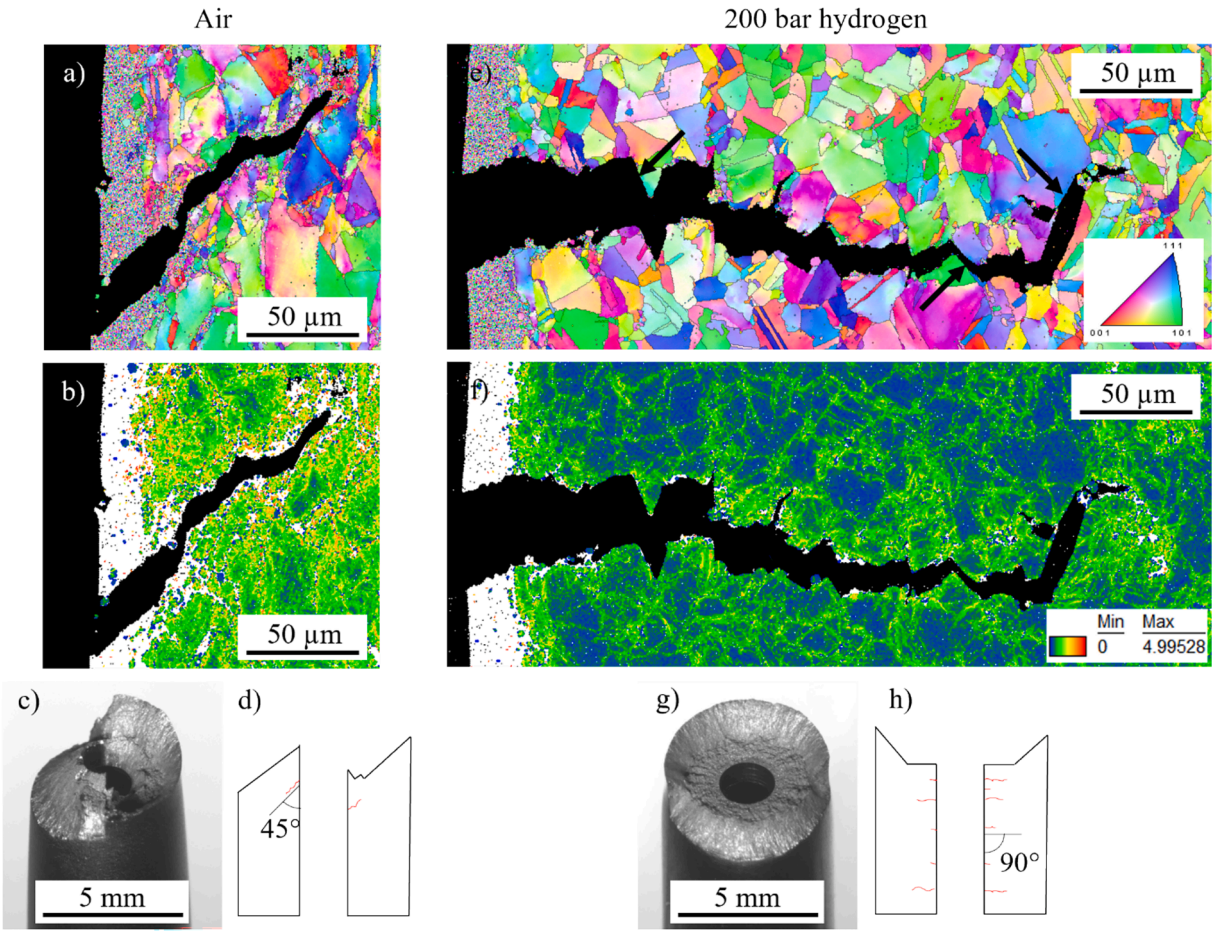

Fig. 7. Inverse pole figure (IPF) map (a, e) and kernel average misorientation (KAM) map (b, f) of secondary cracks on wrought hollow specimens tested in air and tested with 200 bar hydrogen pressure, macro images of the specimens (c, g) and sketched section through the specimens with illustrated crack growth direction (d, h). Intergranular crack path marked with arrows.

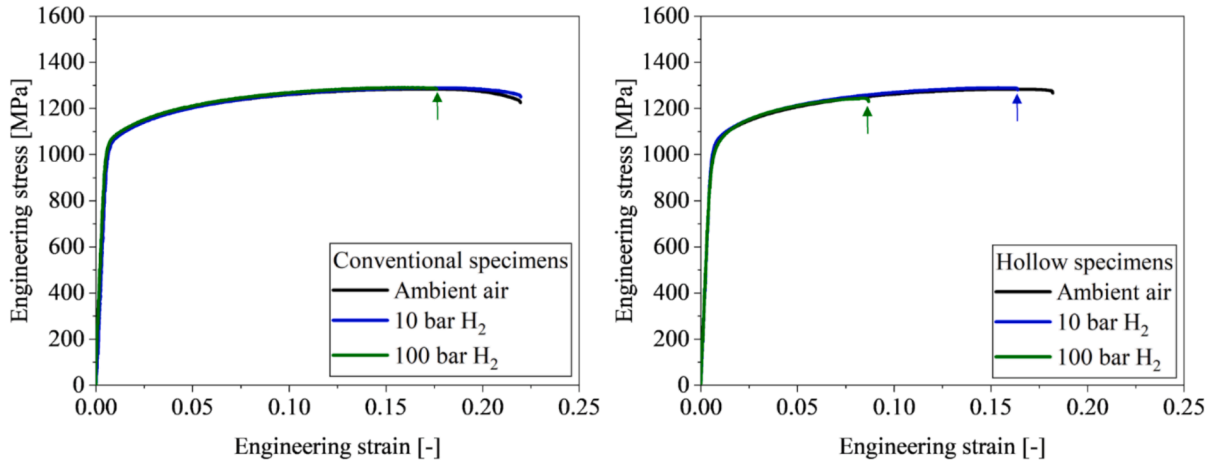

Fig. 8. Tensile tests of alloy 718 SLM at different hydrogen gas pressures in autoclave system on conventional specimens (left) and on hollow specimens (right). Arrows mark the point of failure.

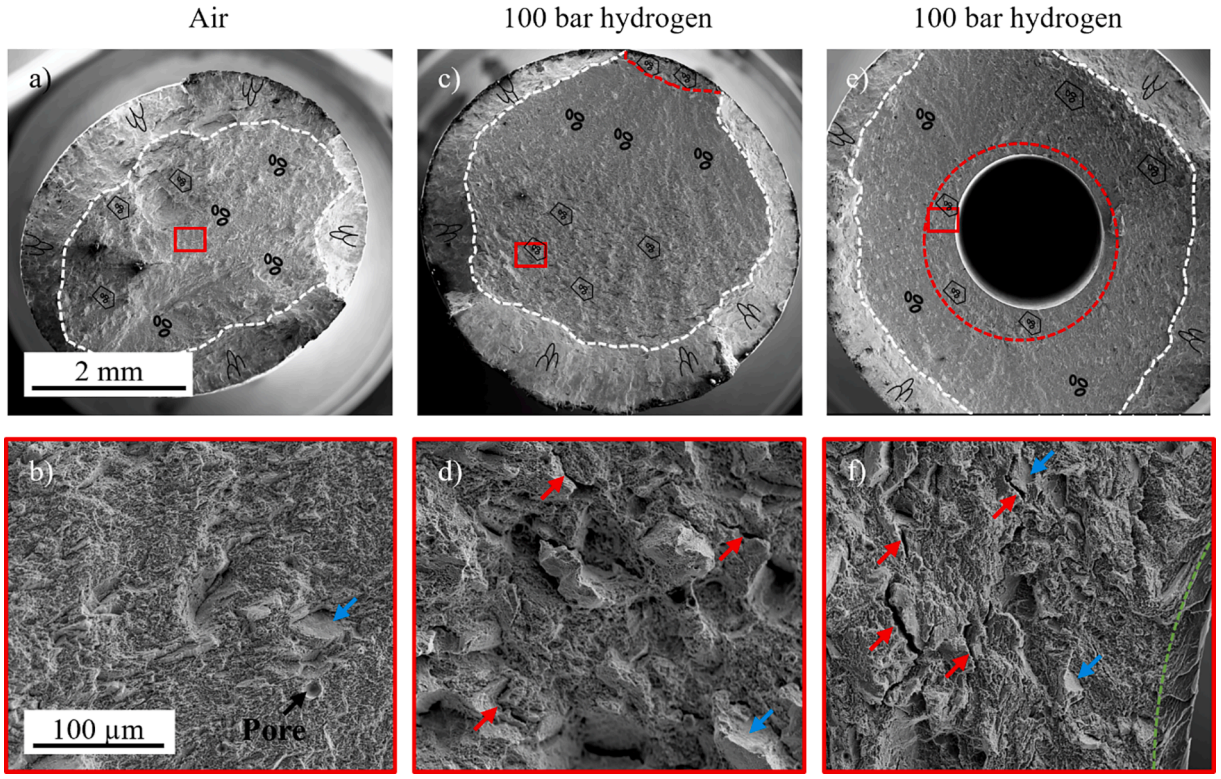

Fig. 9. Fracture surfaces of additive manufactured alloy 718: Conventional specimen tested in air (a, b), conventional specimen tested in 100 bar hydrogen (c, d) and hollow specimen tested in 100 bar hydrogen (e, f). (Fractographic symbols based on [37]). Red arrows mark secondary cracks and blue arrows flat surfaces.

shows shear in 45°-direction and almost no dimples. It is suspected that this is caused by plastic deformation before testing resulting from the deep hole drilling process. The processing of the borehole is a significant subject that is addressed in-depth in the subsequent section of the discussion.

4. Discussion

4.1. Manufacturing process and inner roughness

Although the hollow specimen technique is a simple testing technique and requires little investment, it also has its challenges, starting with specimen production. The axial hole of the specimen can be manufactured using various methods. For example, Ogata used electrical-discharging and wire-cut, but also mentioned that the molten surface in the hole should be removed by further processing. He uses honing and axial polishing to achieve a roughness of Rz ≈ 2 µm and Rz ≈ 3 µm, respectively [39]. The deep-hole drilling used in this work has already achieved a low roughness of Rz = 1.32 µm and does not produce a molten surface. Nevertheless, the material can be cold formed at the surface of the hole due to the drilling process (Fig. 9f), and residual stresses can occur [40] or circumferential grooves can be introduced [22]. These could be reduced in future by a further processing step such as honing or polishing. However, honed specimens were not used in this work due to the poorer surface roughness (Fig. 2). For alloy 718 investigated in this study, the surface roughness achieved by deep hole drilling was Ra = 0.23 µm (Fig. 2) which fulfills the requirements of ASTM G129 [41] specifying a surface roughness of RMS < 0.25 µm (RMS ≈ Ra) for specimens to be tested in gaseous H_2.

4.2. Hydrogen sensitivity of conventional and hollow specimens

Another aspect to consider is the comparison of material properties obtained from different specimen geometries, i.e. CS and HS. In a study by Michler et al. [27] various austenitic steels were examined, and it was found that there was no difference in the yield strength and tensile strength values between the HS and the CS, both in air and in hydrogen gas. However, there were differences in the values of the reduction of area (RA) between the CS and HS. In air the RA of CS was higher than that of HS, while in hydrogen, the RA of CS was lower than that of HS.

This effect was investigated in this work for the alloy 718 at various hydrogen pressures. In addition, the elongation to failure ε_f was evaluated as a measure of hydrogen embrittlement. The plot of ε_f versus pressure in Fig. 10a shows that the HS tested in air has lower elongation to failure than the CS. But this difference in ε_f remains almost constant under hydrogen gas with increasing pressure. The

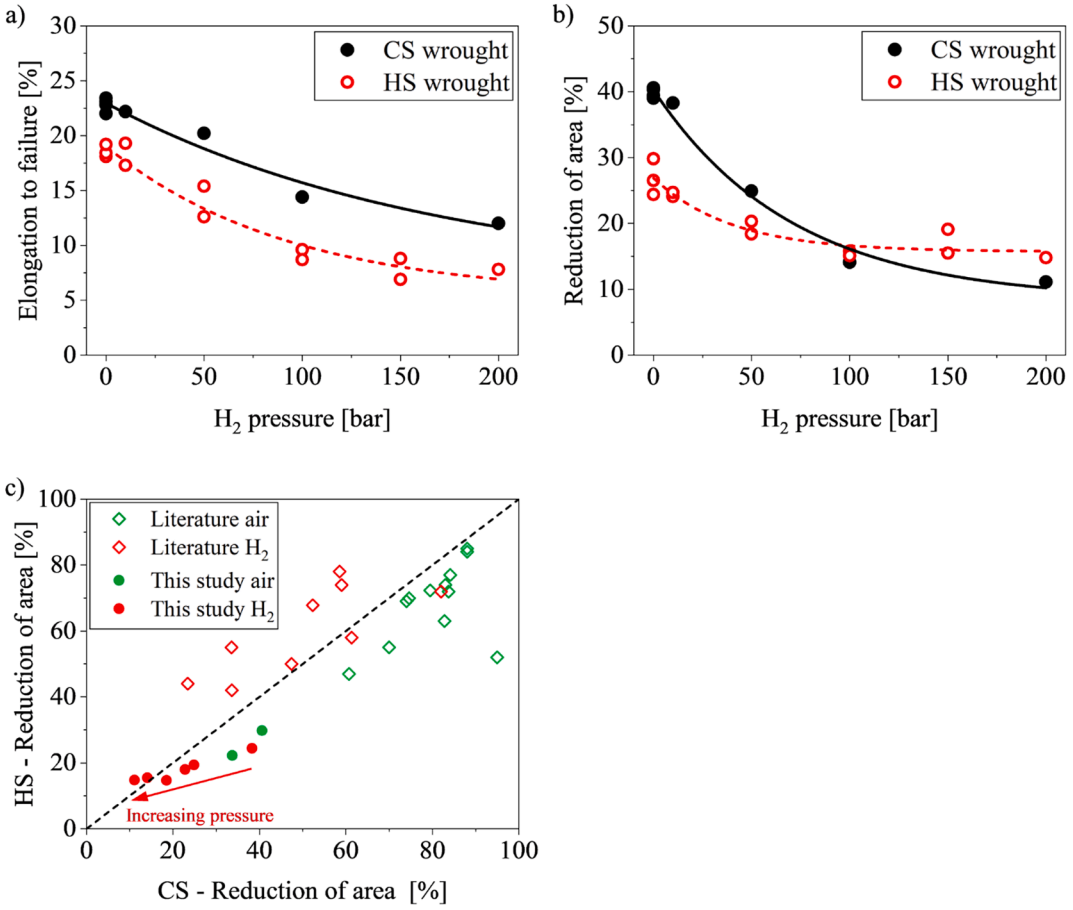

Fig. 10. Elongation to failure (a) and reduction of area (b) over hydrogen pressure for conventional specimens (CS) and hollow specimens (HS) (Fit with exponential growth function with time constant parameter). (c) Comparison of the reduction of area of CS and HS from this work with data from Michler et al. for austenitic steels [27]. The arrow indicates increasing hydrogen pressure of the experiments.

elongation to failure is therefore a suitable indicator for evaluating the influence of hydrogen. For the reduction of area (Fig. 10b), the HS in air also shows a lower value than the CS in air. However, with increasing hydrogen pressure the curve of the HS intersects with the curve of the CS. This means that the reduction of area of HS reacts less sensitive to hydrogen.

To compare the results measured from tests with hydrogen atmosphere to tests in air, the relative elongation to failure $R\varepsilon_f = \frac{\varepsilon_{f,H_2}}{\varepsilon_{f,air}} x100$ [%] and relative reduction of area $RRA = \frac{RA_{H_2}}{RA_{air}} x100$ [%] can be calculated, where 100 % means no influence of hydrogen. In the following the average of reference experiments to 200 bar hydrogen experiments is compared. This results for the HS in $R\varepsilon_{f\,HS,200} = 42$ % and for the CS in $R\varepsilon_{f\,CS,200} = 52.6$ %, which indicates a higher hydrogen susceptibility for the HS. For the relative reduction of area the results are $RRA_{TS,200} = 55$ % for the HS and in $RRA_{CS,200} = 27.9$ % for the CS, which indicates significantly higher hydrogen susceptibility for the CS. However, the different values measured in air have a major influence on this result.

Fig. 10c shows the comparison of the reduction of area of HS and CS. The centerline indicates equal results for both specimens' geometries. For comparison, the results from Michler et al. [27] for austenitic steels were added. It can be seen that for all materials, the values in air are below the centerline, while the results with hydrogen tend to be above it. The results from this work show a trend from the experiments in air towards the center line and beyond with increasing hydrogen pressure. This can be explained by the fact that almost no hydrogen embrittlement occurs at the low pressure of 10 bar. With increasing pressure and increasing embrittlement, the points move towards the center line.

4.3. Failure mechanisms in conventional and hollow specimens

The different mechanical properties discussed before indicate a different damage behavior of the two specimen geometries, both in air and under the influence of hydrogen, which is illustrated in Fig. 11. The damage of the CS is determined by void nucleation, coalescence and growth from the center of the specimen, where the highest hydrostatic stresses occur. Due to the large distance between the center of the specimen and the outer surface, the specimen can strongly neck locally before shear fracture occurs (Fig. 5a).

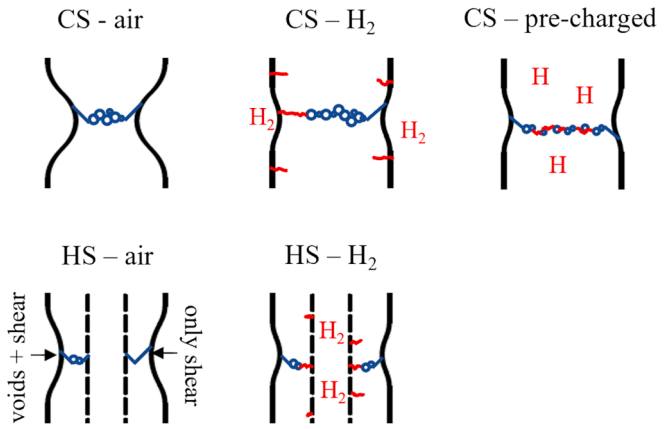

Fig. 11. Schematic of failure mechanisms in conventional and hollow specimens in air, with pressurized hydrogen gas and hydrogen pre-charged. Voids are represented by blue circles, shear fractures are depicted by blue lines in a 45° direction, and hydrogen-assisted cracks are shown in red.

On the fracture surface of the HS tested in air, void nucleation occurs in the wall, somewhat closer to the borehole (Fig. 6a). However, the dimpled area is not distributed around the entire borehole as expected, but only locally. Once the damage and stresses reach a critical point, a catastrophic shear fracture happens. This fracture starts at the damaged area through void nucleation and extends across the entire specimen cross-section. This premature shear failure means that the specimen fails before severe necking can take place. Thus, the constriction of the HS is strongly determined by the transverse contraction over the entire gauge length and not as much by a localization of the plastic deformation as for the CS.

Under hydrogen, both, CS and HS show reduced necking and elongation at break, because hydrogen-induced cracks initiate at the surface in contact with the hydrogen gas and grow perpendicular to the loading direction (Fig. 5e and Fig. 6e). As the pressure increases, more flat surfaces appear on the fracture surface in the area of the crack initiation, indicating the fracture of twin boundaries or slip planes. This mechanism fits the hydrogen enhanced decohesion (HEDE) theory according to Troiano which states that interatomic hydrogen reduces the cohesive bonding strength within the metal lattice [42]. The hydrogen assisted cracks grow into the area damaged by void coalescence, finally leading to an overload shear rupture. This change of failure initiation from void coalescence within the material in air to sub-critical cracks from the surface with hydrogen was also observed by E. Martínez-Pañeda et al. on notched tensile specimens of nickel-based alloy Monel K-500 with electrochemical hydrogen charging. The results were thoroughly discussed, supported by phase field modeling. The simulation revealed that cracks can initiate within just 40–60 % of the test duration, causing deeper hydrogen penetration along the cracks [43]. However, since this change in the damage mechanism was observed in HS and CS, it does not explain the differences between the specimen geometries.

However, there is a difference between the location of crack initiation under hydrogen and the location of necking (Fig. 5e and Fig. 6e). In the case of CS, there is a competition between necking and hydrogen-induced cracks, as both occur at the outer surface. In the case of HS, on the other hand, the specimen can neck from the outside, while hydrogen-induced cracks only compete with the necking on the inside of the specimen. This competition has also been discussed by Michler et al. [27], who additionally found that in the case of HS, necking mainly occurs from the outside and not from the borehole. Due to the small distance between hydrogen enhanced crack initiation at the surface of the borehole and the region damaged by void coalescence, the crack only needs to grow a short distance. This leads to early fracture and low elongation to failure for the HS. In addition, the necking, which mainly occurs from the outside surface, is not directly affected by hydrogen which leads to lower reduction of area.

In contrast to in-situ hydrogen charging, the pre-charged specimen already contains atomic hydrogen in the material. This allows hydrogen to directly attack at the voids that nucleate inside the specimen. Consequently, the crack does not propagate from the outer surface to the inside, as it does under in-situ hydrogen charging. Instead, hydrogen damage initiates from the inside. This can also be confirmed by the fact that residual shear fractures can be seen around the entire circumference of the pre-charged specimen Fig. 5c.

4.4. Multiaxial stresses in hollow specimens

Another reason for this difference between CS and HS may be the stresses in the specimen caused by internal pressure. While the CS is completely surrounded by pressurized hydrogen gas, which leads to a hydrostatic stress state, the gas pressure in the HS is only present inside the borehole. This leads to a multi-axial stress state for the HS. For a rotationally symmetrical body such as the hollow specimen, the elastic stress distribution caused by an internal pressure can be calculated using the following equations [44].

$$\sigma_t = p_i \frac{r_i^2}{r_o^2 - r_i^2}\left(\frac{r_o^2}{r_x^2} + 1\right) \tag{1}$$

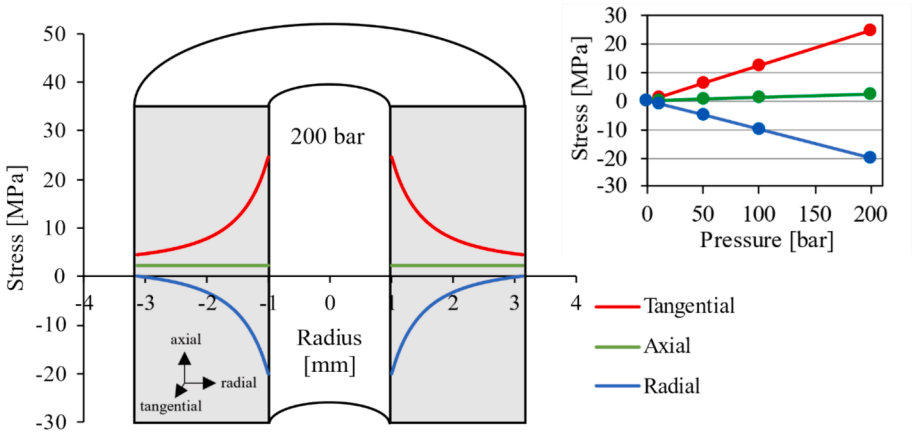

Fig. 12. Distribution of tangential, axial and radial stresses in a hollow specimen with an internal pressure of 200 bar plotted over the wall thickness; the diagram at the top right shows the influence of the gas pressure on the stresses at $x = 1$.

$$\sigma_r = -p_i \frac{r_i^2}{r_o^2 - r_i^2}\left(\frac{r_o^2}{r_x^2} - 1\right) \tag{2}$$

$$\sigma_a = p_i \frac{r_i^2}{r_o^2 - r_i^2} \tag{3}$$

Where σ_t, σ_r and σ_a are the tangential, radial, and axial stress components, respectively. p_i and p_o are the inner and outer pressure, r_i and r_o are the inner and outer radius and r_x is the radius at position x. The equivalent stress σ_v can be calculated using the following equation [44]

$$\sigma_v = \sqrt{\frac{(\sigma_1 - \sigma_2)^2 + (\sigma_2 - \sigma_3)^2 + (\sigma_3 - \sigma_1)^2}{2}} \tag{4}$$

Fig. 12 visualizes the stress distribution within the wall thickness of a hollow specimen. The graph is plotted for an internal pressure of 200 bar, while the small diagram at the top right of Fig. 12 shows the dependence of the stress at the inner surface as a function of the gas pressure. The diagram for 200 bar internal pressure shows that the axial stress is homogeneously distributed over the specimen cross-section with $\sigma_a = 2.3$ MPa. It directly affects the determined yield and ultimate strength. However, it is with 0.2 % of the yield strength $R_{p0.2,CS,air} = 1166 \pm 18.2$ MPa very small and falls within the scatter of the experiments. The radial and tangential stresses, on the other hand, decrease towards the outside of the specimen down to 0 MPa and 4.7 MPa, respectively. The highest stresses occur at the surface of the bore with $\sigma_t = 24.6$ MPa and $\sigma_r = -20$ MPa. With Equation (4), the calculated equivalent stress at the surface of the hole is $\sigma_v = 38.6$ MPa. This equivalent stress corresponds to about 3.3 % of the materials yield strength, which is also comparatively low, but could have a slight influence on the necking behavior of hollow specimens. Nevertheless, it is crucial to carefully analyze these multi-axial stresses for materials with low yield strength and for higher gas pressures. This is because the stresses increase linearly with the pressure, as can be seen in Fig. 12.

Ogata carried out a more comprehensive finite element analysis and found that the yield strength and tensile strength are not affected by the bore hole, but the elongation to failure decreases with increasing hole diameter. This effect is further enhanced by an internal pressure of 1000 bar [39]. Therefore, the borehole diameter should be small and the difference to conventional specimens in elongation should be considered at high pressures.

4.5. Effect of additive manufacturing on hydrogen embrittlement

Alloy 718 wrought and SLM show a comparably susceptibility to hydrogen embrittlement (Fig. 13a). At 10 bar hydrogen pressure, the influence of hydrogen is small and slightly more pronounced in RRA than in $R\varepsilon_f$. At 100 bar pressure, both parameters show comparable hydrogen damage. This result is at first surprising, as the microstructures of the two manufacturing processes differ significantly, see Fig. 3. However, looking at the hydrogen diffusion in alloy 718 for different manufacturing processes and heat treatment states, it can be seen that these do not have a major influence on hydrogen diffusion [5,33,45,46]. For alloy 718 SLM and LBPF (laser powder bed fusion), diffusion rates were measured that match very well with the conventional manufactured material [12,46,47], see Fig. 13b.

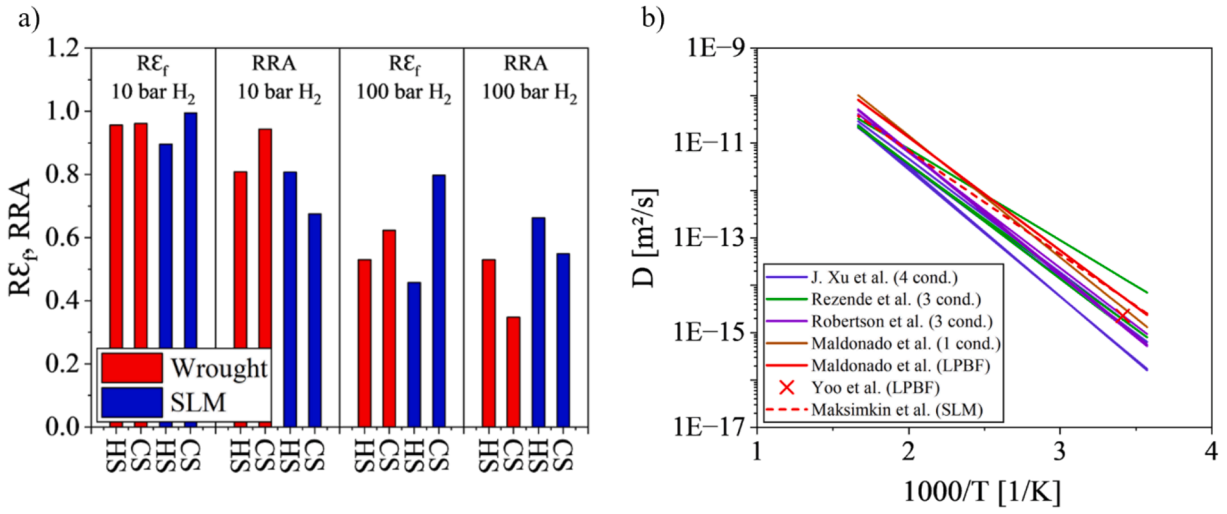

Fig. 13. A) Comparison of the relative elongation at fracture $R\varepsilon_f$ and the relative reduction of area RRA for alloy 718 wrought and SLM. b) Diffusion rates for different conditions of conventional alloy 718 and additive manufactured material (SLM and LPBF). Data from [5,12,33,45–47].

5. Conclusions

Three different techniques were used to conduct slow strain rate tensile tests on alloy 718 in wrought and additively manufactured state. Depending on the test method and test conditions, low to high hydrogen embrittlement was observed. Although the microstructures of the two manufacturing processes differ, no significant difference in hydrogen embrittlement could be detected. The test methods were examined regarding the determined mechanical parameters and the failure mechanisms.

The autoclave technique, using conventional cylindrical specimens, showed reduced elongation to failure with increasing hydrogen pressure. Fracture changed from typical cup and cone fracture in air to a combination of hydrogen assisted crack from the outer surface and void nucleation from the inside.

The hollow specimen technique offers a simple alternative to the autoclave technique. It showed a significant effect of hydrogen on the elongation to failure. The strength values determined are in good agreement with conventional specimens. The elongation to failure of hollow specimens is slightly lower in air and in hydrogen. Possible influencing factors were investigated.

- A higher surface roughness was measured in the borehole than on the outside, although this is still within the specifications of ASTM G129 [41].
- The inner pressure causes multi-axial stresses in the material. An estimation of the equivalent stress at 200 bar in the hollow specimens is relatively small with approx. 3.3 % of the yield strength of alloy 718. Attention should be paid to higher pressures and materials with low yield strength.
- It is most likely that the differences in elongation to failure are caused by a different damage behavior. The fact that in hollow specimens voids cannot nucleate in the center of the specimen as in conventional ones, but in the wall thickness around the hole, can lead to asymmetric damage and premature shear fracture.

Pre-charging with hydrogen at 350 °C and 100 bar until saturation showed the strongest embrittlement. The investigation of the fracture surfaces showed a clear difference to the in-situ techniques. Pre-charging leads to hydrogen damage from the inside. The hydrogen-influenced portion of the fracture surface was particularly large here.

In the future, the hollow specimen technique might offer new possibilities in the investigation of hydrogen embrittlement, such as cost-effective material screening on a large scale, simple cooling and heating of the specimen from the outside and to measure changes in hydrogen pressure due to small hydrogen absorption. However, it will not replace standardized tests in the autoclave and attention must be paid to the differences in the measured elongation to failure. Specimens' ex-situ pre-charged showed a significantly different damage behavior. A direct comparison to in-situ tests is not possible.

CRediT authorship contribution statement

Fabien Ebling: Writing – original draft, Project administration, Methodology, Investigation, Data curation, Conceptualization. **Philipp Bratsch:** Writing – review & editing, Investigation, Data curation. **Stefan Wagner:** Writing – review & editing, Supervision. **Astrid Pundt:** Writing – review & editing, Supervision. **Johannes Preußner:** Writing – review & editing, Supervision. **Heiner Oesterlin:** Writing – review & editing, Supervision. **Ken Wackermann:** Writing – review & editing, Supervision, Funding acquisition. **Thorsten Michler:** Writing – review & editing, Supervision.

Declaration of competing interest

The authors declare that they have no known competing financial interests or personal relationships that could have appeared to influence the work reported in this paper.

Acknowledgements

This study was financially supported by the German Federal Ministry for Economic Affairs and Climate Action (BMWK) as part of the aviation research program LuFo VI-1 under grant number 20M1904E (AdHyBau). The authors would like to thank Karin Hintz and Sabine Oeser for the preparation of metallographic samples and for taking micrographs using optical microscopy, SEM and EBSD.

Appendix

Table 1
Results of slow strain rate tensile tests.

Geometry	Condition	Medium	Pressure [bar]	Pre-charging	$R_{p0.2}$ [MPa]	R_m [MPa]	ε_f [MPa]	RA [%]
HS	Wrought	Air	0	no	1173	1403	18.1	29.8
HS	Wrought	N2	0	no	1179	1396	18.4	26.5
HS	Wrought	N2	0	no	1181	1406	19.2	24.4
HS	Wrought	H2	10	no	1180	1399	17.3	24.1
HS	Wrought	H2	10	no	1184	1407	19.3	24.7
HS	Wrought	H2	50	no	1175	1385	12.6	18.4
HS	Wrought	H2	50	no	1168	1393	15.4	20.3
HS	Wrought	H2	100	no	1175	1372	9.6	15.8
HS	Wrought	H2	100	no	1182	1367	8.7	15.1
HS	Wrought	H2	150	no	1174	1372	8.8	19.1
HS	Wrought	H2	150	no	1174	1354	6.9	15.5
HS	Wrought	H2	200	no	1183	1351	7.8	14.8
CS	Wrought	Air	0	no	1168	1414	23.1	40.6
CS	Wrought	Air	0	no	1136	1411	22	40.3
CS	Wrought	Air	0	no	1177	1422	23.4	39.4
CS	Wrought	Air	0	no	1183	1422	22.8	39
CS	Wrought	H2	10	no	1170	1406	22.2	38.3
CS	Wrought	H2	50	no	1160	1416	20.2	24.9
CS	Wrought	H2	100	no	1168	1410	14.4	14.1
CS	Wrought	H2	200	no	1193	1394	12	11.1
CS	Wrought	Air	0	yes	1113	1354	8.5	12.6
HS	SLM	Air	0	no	1036	1284	17.52	22.2
HS	SLM	H2	10	no	1044	1290	15.7	18
HS	SLM	H2	100	no	1012	1244	8.02	14.7
CS	SLM	Air	0	no	1042	1281	21.3	33.7
CS	SLM	H2	10	no	1049	1290	21.2	22.8
CS	SLM	H2	100	no	1047	1292	17	18.5

Data availability

Data will be made available on request.

References

[1] Johnson WH. II. On some remarkable changes produced in iron and steel by the action of hydrogen and acids. Proc R Soc London 1875;23(156–163):168–79. https://doi.org/10.1098/rspl.1874.0024.
[2] Hirth JP. Effects of hydrogen on the properties of iron and steel. Metall Trans A 1980;11(6):861–90. https://doi.org/10.1007/BF02654700.
[3] Pundt A, Kirchheim R. Hydrogen in metals: microstructural aspects. Annu Rev Mater Res 2006;36(June):555–608. https://doi.org/10.1146/annurev.matsci.36.090804.094451.
[4] Oriani RA. The physical and metallurgical aspects of hydrogen in. Metals 1993.
[5] Rezende MC, Araujo LS, Gabriel SB, Dos Santos DS, De Almeida LH. Hydrogen embrittlement in nickel-based superalloy 718: relationship between γ' + γ'' precipitation and the fracture mode. Int J Hydrogen Energy 2015;40(47):17075–83. https://doi.org/10.1016/j.ijhydene.2015.07.053.
[6] Zhang Z, Obasis G, Morana R, Preuss M. Hydrogen assisted crack initiation and propagation in a nickel-based superalloy. Acta Mater, 2016;113:272–83. https://doi.org/10.1016/j.actamat.2016.05.003.
[7] Ogawa Y, Takakuwa O, Okazaki S, Funakoshi Y, Matsuoka S, Matsunaga H. Hydrogen-assisted fatigue crack-propagation in a Ni-based superalloy 718, revealed via crack-path crystallography and deformation microstructures. Corros. Sci. 2020;174(March). https://doi.org/10.1016/j.corsci.2020.108814.
[8] Lu X, Wang D, Wan D, Zhang ZB, Kheradmand N, Barnoush A. Effect of electrochemical charging on the hydrogen embrittlement susceptibility of alloy 718. Acta Mater 2019;179:36–48. https://doi.org/10.1016/j.actamat.2019.08.020.

[9] Demetriou V, Robson JD, Preuss M, Morana R. Study of the effect of hydrogen charging on the tensile properties and microstructure of four variant heat treatments of nickel alloy 718. Int J Hydrogen Energy 2017;42(37):23856–70. https://doi.org/10.1016/j.ijhydene.2017.02.149.

[10] Liu L, Tanaka K, Hirose A, Kobayashi KF. Effects of precipitation phases on the hydrogen embrittlement sensitivity of inconel 718. Sci Technol Adv Mater 2002;3 (4):335–44. https://doi.org/10.1016/S1468-6996(02)00039-6.

[11] Jothi S, Merzlikin SV, Croft TN, Andersson J, Brown SGR. An investigation of micro-mechanisms in hydrogen induced cracking in nickel-based superalloy 718. J Alloys Compd 2016;664:664–81. https://doi.org/10.1016/j.jallcom.2016.01.033.

[12] Yoo J, Kim S, Cheol M, Park H. Investigation of hydrogen embrittlement properties of Ni-based alloy 718 fabricated via laser powder bed fusion. Int J Hydrogen Energy 2022;47(43):18892–910. https://doi.org/10.1016/j.ijhydene.2022.04.045.

[13] Mohandas NK, Giorgini A, Vanazzi M, Riemslag T, Scott SP, Popovich V. Hydrogen embrittlement of inconel 718 manufactured by laser powder bed fusion using sustainable feedstock: effect of heat treatment and microstructural anisotropy. Metals (Basel) 2023;13(2). https://doi.org/10.3390/met13020418.

[14] Tarzimoghadam Z, Ponge D, Klöwer J, Raabe D. Hydrogen-assisted failure in Ni-based superalloy 718 studied under in situ hydrogen charging: the role of localized deformation in crack propagation. Acta Mater 2017;128:365–74. https://doi.org/10.1016/j.actamat.2017.02.059.

[15] Matsuo T, et al. Development of new strain gage for high-pressure hydrogen gas use. Exp Mech 2014;54(3):431–42. https://doi.org/10.1007/s11340-013-9816-4.

[16] Jewet RP, Walter RJ, Chandler WT, Frohmberg RP. Hydrogen environment embrittlement of metals. NASA Contract Rep CR-2163 1973.

[17] Ogata T. Influence of 70 MPa hydrogen gas on SUS 630 from 77 K to 373 K by simple testing method. Am Soc Mech Eng Press Vessel Pip Div PVP 2018;6B-2018: 1–5. https://doi.org/10.1115/pvp2018-84462.

[18] Nakamura J, Miyahara M, Omura T, Semba H, Wakita M, Otome Y. Degradation of fatigue properties in high pressure gaseous hydrogen environment evaluated by cyclic pressurization tests. Procedia Eng 2010;2(1):1235–41. https://doi.org/10.1016/j.proeng.2010.03.134.

[19] Du J, Ming H, Wang J, Han EH. Hydrogen embrittlement of 20# seamless steel in medium and low pressure gaseous hydrogen. Mater Lett 2023;334(December 2022):133734. https://doi.org/10.1016/j.matlet.2022.133734.

[20] Ueno A, Benjamin G. Effect of high-pressure H2 gas on tensile and fatigue properties of stainless steel SUS316L by means of the internal high-pressure H2 gas method. Procedia Struct Integr 2019;19:494–503. https://doi.org/10.1016/j.prostr.2019.12.053.

[21] Wan HJ, Wu XQ, Ming HL, Wang JQ, Han EH. Effects of hydrogen charging time and pressure on the hydrogen embrittlement susceptibility of X52 pipeline steel material. Acta Metall Sin (English Lett) 2023:0123456789. https://doi.org/10.1007/s40195-023-01625-5.

[22] Michler T, Ebling F, Oesterlin H, Fischer C, Wackermann K. Comparison of tensile properties of X60 pipeline steel tested in high pressure gaseous hydrogen using tubular and conventional specimen. Int J Hydrogen Energy 2022;47(81):34676–88. https://doi.org/10.1016/j.ijhydene.2022.07.211.

[23] Faucon LE, Boot T, Riemslag T, Scott SP, Liu P, Popovich V. Hydrogen-accelerated fatigue of API X60 pipeline steel and its weld. Metals (Basel) 2023;13(3). https://doi.org/10.3390/met13030563.

[24] Ogata T. Hydrogen environment embrittlement on austenitic stainless steels from room temperature to low temperatures. IOP Conf Ser Mater Sci Eng 2015;102 (1). https://doi.org/10.1088/1757-899X/102/1/012005.

[25] Ogata T. Influence of high pressure hydrogen environment on tensile and fatigue properties of stainless steels at low temperatures. AIP Conference Proceedings 2012;1435(2012):39–46. https://doi.org/10.1063/1.4712078.

[26] Ebling F, Oesterlin H, Wackermann K, Primus D, Rehme O. Hydrogen effects on low cycle fatigue of IN718 at RT and 77K using the tubular specimen technique. Proc Fourth Int Conf Met Hydrog 2022:10.

[27] Michler T, Freitas T, Oesterlin H, Fischer C, Wackermann K, Ebling F. Tensile testing in high pressure gaseous hydrogen using conventional and tubular specimens: austenitic stainless steels. Int J Hydrogen Energy 2023;48(65):25609–18. https://doi.org/10.1016/j.ijhydene.2023.03.248.

[28] Ogata T. Evaluation of hydrogen embrittlement by internal high-pressure hydrogen environment in specimen. Nippon Kinzoku Gakkaishi/Journal Japan Inst Met 2008;72(2):125–31. https://doi.org/10.2320/jinstmet.72.125.

[29] Lee JA. Hydrogen embrittlement of nickel, cobalt and iron-based superalloys. Gaseous hydrogen embrittlement of materials in energy technologies Volume 1: The problem, its characterisation and effects on particular alloy classes 2012:624–67. https://doi.org/10.1533/9780857093899.3.624.

[30] Chandler WT, Walter RJ. Testing to determine the effect of high- pressure hydrogen environments on the mechanical properties of metals. Hydrogen Embrittlement Testing, ASTM STP 543, American Society for Testing and Materials 1974:170–97.

[31] Michler T, Schweizer F, Wackermann K. Review on the influence of temperature upon hydrogen effects in structural alloys. Metals (Basel) Mar. 2021;11(3):423. https://doi.org/10.3390/met11030423.

[32] Lewandowski JJ, Lowhaphandu P. Effects of hydrostatic pressure on mechanical behaviour and deformation processing of materials. Int Mater Rev, 1998;43(4): 145–87. https://doi.org/10.1179/imr.1998.43.4.145.

[33] Xu J, Sun XK, Liu QQ, Chen WX. Hydrogen permeation behavior in IN718 and GH761 superalloys. Metall Mater Trans A 1994;25(3):539–44. https://doi.org/10.1007/BF02651595.

[34] Ebling F, Wackermann K. Gaseous hydrogen charging and fatigue testing on IN718. Am Soc Mech Eng Press Vessel Pip Div PVP 2022;4-B:1–5. https://doi.org/10.1115/PVP2022-84184.

[35] Oradei-Basile A, Radavich JF. A current T-T-T diagram for wrought alloy 718, in Superalloys 718, 625 and Various Derivatives (1991), 1991, 325–335. 10.7449/1991/Superalloys_1991_325_335.

[36] Ling L-S-B, et al. Effects of the γ″-Ni3Nb phase on mechanical properties of inconel 718 superalloys with different heat treatments. Materials (Basel) 2019;13(1): 151. https://doi.org/10.3390/ma13010151.

[37] "FractoGraphics v0.60," Fraktographische Datenbank. www.fraktographie.bam.de.

[38] An B, Itouga H, Iijima T, San Marchi C, Somerday B. Hydrogen-assisted twin boundary fracture of type 304 austenitic stainless steel at low temperature investigated by scanning probe microscopy, in Volume 6B: Materials and Fabrication, 2013, 1–6. 10.1115/PVP2013-97355.

[39] Ogata T, Ono Y. Influence of roughness of inner surface of simple mechanical testing method to evaluate influence of high pressure hydrogen gas, Am. Soc. Mech. Eng. Press. Vessel. Pip. Div. PVP, 6B-2019, pp. 1–6, 2019, 10.1115/PVP2019-93492.

[40] Oesterlin H, Michler T, Fischer C, Schönborn S. Low cycle fatigue testing of X60 pipeline steel in high pressure gaseous hydrogen using tubular and conventional specimens. Int J Hydrog Energy 2024.

[41] "ASTM G129-00(2013): Standard Practice for Slow Strain Rate Testing to Evaluate the Susceptibility of Metallic Materials to Environmentally Assisted Cracking," ASTM Int., no. Book of Standards Volume: 03.02, 2013, doi: 10.1520/G0129-00R13.

[42] Troiano AR. The role of hydrogen and other interstitials in the mechanical behavior of metals. Trans Am Soc Met 1960;52:54–80. https://doi.org/10.1007/s13632-016-0319-4.

[43] Martínez-Pañeda E, Harris ZD, Fuentes-Alonso S, Scully JR, Burns JT. On the suitability of slow strain rate tensile testing for assessing hydrogen embrittlement susceptibility. Corros Sci 2020;163(November 2019):108291. https://doi.org/10.1016/j.corsci.2019.108291.

[44] Altenbach H. Holzmann/Meyer/Schumpich Technische Mechanik Festigkeitslehre. Wiesbaden: Springer Fachmedien Wiesbaden; 2022. doi: 10.1007/978-3-658-41029-2.

[45] Robertson WM. Hydrogen permeation and diffusion in inconel 718 and incoloy 903. Metall Trans A 1977;8A(November):1709–12.

[46] Santos Maldonado C, Zafra A, Pañeda EM, Sandmann P, Morana R, Pham M-S. Inuence of dislocation cells in the hydrogen diffusivity, trapping and embrittlement of wrought and additively manufactured Inconel 718. Commun Mater 2024. https://doi.org/10.1038/s43246-024-00654-6.

[47] Maksimkin IP, et al. Effect of hydrogen on the structure and mechanical properties of 316L steel and inconel 718 alloy processed by selective laser melting, Materials (Basel)., vol. 15, no. 14, 2022, doi: 10.3390/ma15144806.